Journal of Electroanalytical Chemistry 975 (2024) 118795

Contents lists available at ScienceDirect

Journal of Electroanalytical Chemistry

journal homepage: www.elsevier.com/locate/jelechem

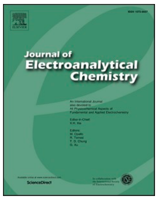

Electrochemical evaluation of the real surface area of copper-zinc alloys

Oleg I. Zaytsev [a], Margarita A. Belokozenko [a,b], Grigorii P. Lakienko [a,b], Eduard E. Levin [b,c,**], Victoria A. Nikitina [a,*], Sergey Y. Istomin [b]

[a] *Center for Energy Science and Technology, Skolkovo Institute of Science and Technology, Nobel Street 3, 143026 Moscow, Russia*
[b] *Lomonosov Moscow State University, Leninskie Gory 1/3, 119991 Moscow, Russia*
[c] *FSRC "Crystallography and photonics" of NRC «Kurchatov Institute», Leninsky Prospekt 59, 119333 Moscow, Russia*

ARTICLE INFO

Keywords:
Real surface area
α-brass
Alloys
Electrocatalysis
Electrochemically active surface area
Cyclic voltammetry

ABSTRACT

Accurate measurements of real surface area (RSA) are essential in fundamental electrocatalysis for evaluating the intrinsic activity of various materials. However, existing electrochemical methods for determining RSA values in metallic alloys, particularly those containing active metals, remain underexplored. This study critically assesses the efficacy of capacitance measurement techniques for calculating RSA values in copper-zinc alloys, which are commonly employed as electrocatalysts for CO_2 reduction. We investigate optimal conditions for estimating RSA through cyclic voltammetry, focusing on electrolyte selection and appropriate potential ranges to ensure reliable RSA assessments. Additionally, we emphasize the necessity of using suitable reference samples for accurate specific capacitance calculations. Our findings reveal that potential uncertainties arising from the use of inappropriate reference samples across different Cu-Zn compositions can reach an order of magnitude, rendering them unsuitable for electrocatalytic studies. This research highlights the need for robust surface area quantification techniques to reduce uncertainties in reporting the activities of alloy-based materials in various electrochemical applications.

1. Introduction

Alloy electrocatalysts are promising materials for electrochemical energy conversion. They are commonly used in electrolyzers and fuel cells [1,2]. The addition of a second element in the alloy typically modifies the electronic structure of the catalytic surface, enhancing activity in various processes such as hydrogen evolution and oxidation [3–5], as well as oxygen [6–8] and carbon dioxide [9–12] reduction reactions. In electrocatalytic applications, the real surface area (RSA) or electrochemically active surface area (ECSA) are critical parameters [13], as they indicate the number of active sites involved in complex multistep proton-coupled electron transfer reactions. While the widely used BET method for measuring specific surface area (SSA) provides an approximation of RSA, it often overlooks the presence of electrically disconnected particles in composite electrodes used in practical electrocatalytic measurements. Estimation of RSA is essential for accurately comparing the activity of different electrocatalysts across various research groups.

Established techniques for estimating RSA of noble metals (such as Pt, Au, Rh, Pd, Ir) rely on electrochemical processes, including the underpotential formation of hydrogen and oxygen monolayers, deposition of Cu and Pb adatoms, and CO stripping [13]. RSA calculations are typically derived from analyzing voltammetric or chronoamperometric responses of electrodes, focusing on characteristic adsorption and desorption peaks. Although these methods are based on strong assumptions regarding complete electron transfer between adsorbed species and the electrode surface, as well as averaged surface atom concentrations for polycrystalline electrodes, the resulting RSA values generally align with independent estimates obtained via BET or microscopy techniques.

Determining the RSA for non-noble metals can be particularly challenging. For instance, copper electrodes undergo complex electrochemical surface and bulk reactions, that are difficult to separate from double-layer charging, such as the appearance of OH_{ad} species in alkaline solutions in the underpotential range of Cu_2O formation, reported primarily for single-crystalline surfaces [14–17]. Fortunately, the underpotential deposition (UPD) of metals like lead and thallium onto copper yields well-defined responses that can be utilized to assess the

---

* Corresponding author.
** Corresponding author at: Lomonosov Moscow State University, Leninskie Gory 1/3, 119991 Moscow, Russia.
E-mail addresses: levin@elch.chem.msu.ru (E.E. Levin), v.nikitina@skoltech.ru (V.A. Nikitina).

https://doi.org/10.1016/j.jelechem.2024.118795
Received 2 September 2024; Received in revised form 17 October 2024; Accepted 8 November 2024

roughness of the copper surface [18–21]. For certain transition metal-based materials, specific techniques exist for surface area estimation. For example, the formation of a monolayer of α-$Ni(OH)_2$ hydroxide on nickel electrodes [22–24] or the adsorption of oxalate on nickel hydroxides [25] can provide valuable insights.

Alternatively, double-layer capacitance measurements can be employed to estimate the RSA, provided that a reliable reference value is available. Relying on arbitrary values, such as the typically used values of 20–40 μF cm^{-2}, to estimate RSA for metal electrodes is generally regarded as an unreliable method, lacking proper justification [13]. Accurately determining double-layer capacitance requires identification of a double-layer region in voltammograms of metals and alloys, where faradaic processes, including adsorption, are absent. This condition is not always met, even for noble metals like rhodium and ruthenium [26,27]. For other d-metals, identifying a true double-layer region is particularly difficult due to their propensity for surface oxidation and strong anion adsorption, with voltammetric characteristics being significantly influenced by electrolyte composition [13]. Migrating from aqueous to nonaqueous media only partially addresses the uncertainty surrounding reference capacitance values, as different metals continue to exhibit significant variations in measured values – sometimes up to fourfold [28]. Additionally, the suitability of nonaqueous electrolytes, which typically have lower conductivity, for the electrochemical characterization of highly dispersed and porous materials remains uncertain, and the measured capacitance can also be influenced by the amount of residual water present in the electrolytes.

The estimation of the RSA for alloys is a relatively underexplored topic. When examining noble metal alloys, such as Pt-Rh, more stringent assumptions are required to derive RSA from techniques like hydrogen UPD. In these cases, understanding the surface fraction of the alloy constituents is essential, along with making informed assumptions about their adsorption properties [29–31]. For alloys that include active metals like Zn, Sn, Bi, and Ni, determining RSA through electrochemical methods poses significant challenges. This difficulty arises from the susceptibility to dealloying and surface restructuring, particularly under electrochemical conditions [32–34]. Consequently, electrochemical techniques for RSA determination in these alloys often become limited to measuring charges in the relatively flat regions of the cyclic voltammograms (CVs), while true double-layer behavior is likely absent. Moreover, the capacitance of alloys does not necessarily correlate linearly with their composition, complicating the identification of a reference value for normalizing capacitance values obtained experimentally. Despite these challenges, the literature contains numerous straightforward estimates of RSA for non-noble metal-based alloys [35–39]. These estimates frequently arise in electrocatalytic studies of CO_2 reduction, where researchers either use a reference capacitance value from one of the pure components – such as the capacitance of metallic Pb for the $SnPb_3$ alloy [36] – or that of pure Cu for Cu-Zn alloys [37] or rely on arbitrary values deemed typical for a class of compounds (e.g., a double-layer capacitance of 40 μF cm^{-2} used to calculate the ECSA for CuZnO materials [35]).

In this study, we critically examine the validity of capacitance measurement techniques for calculating the RSA values for Cu-Zn alloys, which are widely utilized as electrocatalysts for CO_2 reduction to multicarbon products [39–45]. Given the promising potential for practical applications due to the unique selectivity of these materials, developing an accurate procedure for estimating RSA is crucial for enabling meaningful comparisons of reported activities across various studies. We emphasize the importance of using an appropriate specific capacitance value for these alloy materials and estimate the potential errors that may arise when using the capacitance of a more noble alloy component as a reference.

2. Experimental

2.1. Preparation of the samples

2.1.1. Copper foam deposition

The deposition of Cu and $Cu_{(Cl)}$ foams is described in full details in [46]. In brief, the two types of foams were deposited from the solutions of 0.075 M $CuSO_4$ + 0.5 M H_2SO_4 (Cu foam) and 0.075 M $CuSO_4$ + 0.05 M KCl + 0.5 M H_2SO_4 ($Cu_{(Cl)}$ foam) at the current density of 3 A cm^{-2} for 30 s on a surface of a commercial copper foil (Goodfellow). After deposition, the samples were washed with a water mist system and dried in a vacuum oven at 70 °C for 30 min. The same procedure of rinsing and drying was applied to all other deposits.

2.1.2. Copper-zinc foam deposition

For the deposition of α-brass foams the following solutions were used: 1) 0.02 M $CuSO_4$ (Component-reaktiv, 99.5 %, $CuSO_4{\cdot}5H_2O$) + 0.027 M $ZnSO_4$ (Component-reaktiv, 99.5 %, $ZnSO_4{\cdot}7H_2O$) + 0.5 M H_2SO_4 (Component-reaktiv, 94.6 %) ($Cu_{70}Zn_{30}$ target composition); 2) 0.2 M $CuSO_4$ + 0.03 M $ZnSO_4$ + 0.3 M $Na_3C_6H_5O_7$ (Sigma Aldrich, ≥99.5 %, $C_6H_5Na_3O_7{\cdot}2H_2O$) + 1 M $(NH_4)_2SO_4$ (Component-reaktiv, 99 %) ($Cu_{90}Zn_{10}$ target composition). About 70 mL of a selected solution was placed into a rectangular glass cuvette. Copper foil and a glassy carbon plate (Fisher Scientific) were used as working and counter electrodes, respectively. The spacing between electrodes was 2 cm. The surface of the working electrode was isolated with a PET tape to obtain working area of 1 cm^2. Prior to deposition, both electrodes were pretreated in 195 g L^{-1} H_2SO_4 at 60 °C, washed with H_2O and dried with Ar in order to remove surface oxide. The cathode was further activated in 17.5 g L^{-1} H_2SO_4 at room temperature. The deposition was done at the current density of 3 A cm^{-2} for 30 s. The current was supplied by a DC power source.

2.1.3. Copper-zinc deposition

The deposition of smooth α-brass coatings ($Cu_{90}Zn_{10}$ target composition) was carried out in a single-compartment three-electrode glass cell in the potentiostatic mode. The cell volume was ~ 70 mL. The following solution was used: 0.02 M $CuSO_4$ + 0.3 M $ZnSO_4$ + 0.01 M H_3BO_3 (Component-reaktiv, 99.9 %) + 0.9 M $K_4P_2O_7$ (Reachem, 96.68 %). Cu foil was used as both the working and counter electrodes. The reference electrode was AgCl/Ag (3 M KCl). The deposition was carried out at –1.3 V (vs. AgCl/Ag (3 M KCl)) with the charge density 10C cm^{-2}. To maintain the constant composition of the deposition solution, it was intensively circulated through the cell with the aid of a peristaltic pump (flow rate 270 mL/min). The volume of the deposition solution reservoir was 800 mL. The potential and charge were controlled by a Metrohm Autolab PGSTAT302N potentiostat.

2.1.4. Commercial foils

The foils of pure copper and brass containing 10 and 33 wt% of Zn were used as received after thorough degreasing by subsequent washing in acetone (Chimmed, >99.8 %), isopropanol (Chimmed, >99.8 %) and ethanol (Chimmed, > 95.0 %) followed by thorough rinsing with MilliQ water.

2.2. Characterization methods

X-ray Diffraction (XRD) patterns of the deposits detached from substrates were collected using Bruker D8 Advance diffractometer (Bragg–Brentano geometry, CuKα radiation, LynxEye XE detector) in the range of 2θ angles 35–100°. The patterns of commercial foils were measured using Bruker D8 Advance diffractometer (Bragg–Brentano geometry, CuKα radiation, LynxEye detector) in the same 2θ range. Phase identification was done by comparing observed peaks with literature data on Cu and Cu–Zn phases [47–49]. The full-profile analysis of XRD patterns of the detached samples was used to determine unit cell parameters and phases relative content within the framework of the Rietveld method [50,51] implemented in DDM 1.95 software package [52,53]. Unit cell parameters of the commercial Cu–Zn foils were determined using the Le Bail method [54] due to complex texture of the samples. XRD patterns after full-profile treatment are given in Fig. S1. Phase characterization of Cu and $Cu_{(Cl)}$ foams is provided in Ref. [46].

Scanning electron microscopy (SEM) images were registered using JEOL JSM 6490 LV (tungsten hairpin gun, 30 kV, Everhart–Thornley (positive bias)) scanning electron microscope. Energy-dispersive X-Ray spectra (EDS) were measured with INCA X-sight (Oxford Instruments) spectrometer. Samples composition was estimated using standardless approach as implemented in Microanalysis suite software v. 17b (Oxford Instruments). Calculated composition of the samples is given in Table S1. Images of Cu and $Cu_{(Cl)}$ foams are given in [46].

Nitrogen adsorption–desorption isotherms were recorded on the TMAX 3H-2000PM2 gas sorption analyzer at –196 °C. All samples were preliminarily outgassed under vacuum at 100 °C for 7 h. The Brunauer–Emmett–Teller (BET) specific surface area (SSA) was determined from the linear plot in the relative pressure range of 0.05–0.3P/P_0. Measurements were repeated at least 3 times for each sample for calculation of mean SSA. Mass of the samples used in measurements was about 100 mg. In order to verify the reliability of the results obtained using low masses of samples, the Quantachrome standard reference material 06500–2001 (alumina) with SSA of 10.24 ± 0.57 m^2/g and a mass of 80 mg was measured several times. The accuracy of determining the area was ~ 10 %. In parallel with the measurement of the sample, the measurement of the standard reference materials was carried out for reliability. The adsorption isotherms for Cu and $Cu_{70}Zn_{30}$ foams are shown in Fig. S2.

2.3. *Electrochemical measurements*

Cyclic voltammetry measurements were performed on dispersed and compact Cu and Cu-Zn samples in four solutions: 0.5 M Na_2SO_4 (Component-reaktiv, >99 %, $Na_2SO_4 \cdot 10H_2O$, pH 5.9), 0.5 M $KHCO_3$ (Sigma Aldrich, >99.7 %, pH 8.8), 0.1 M KOH (Component-reaktiv, 45 wt% solution in water, pH 13), 0.1 M phosphate buffer (PBS, pH 7.4). 0.1 M PBS was prepared by mixing the solutions of 0.5 M K_2HPO_4 (Component-reaktiv, >99.0 %) and 0.5 M KH_2PO_4 (Component-reaktiv, >99.5 %) and diluting them with MilliQ water to reach the target 0.1 M concentration.

The measurements were performed in a glass three-electrode cell with unseparated compartments of working and counter (graphite rod) electrodes. AgCl/Ag (3 M KCl) electrode was used as the reference electrode for the measurements in Na_2SO_4, $KHCO_3$ solutions and PBS. 1 M KOH HgO/Hg electrode was used as the reference electrode for the measurements in 0.1 M KOH solution. The solution was purged with Ar for 30 min before the measurements, and Ar flow was maintained above the solution during the measurements. To prevent contamination of the 0.1 M KOH solution by leached glass constituents [55–57], the solution was prepared and stored in a PTFE flask. During measurements in an electrochemical glass cell, which lasted no longer than 1 h, no changes in the CVs were observed. This stability suggests that leaching of silicates, borates, and aluminates from the glass did not impact the electrochemical data collected during this time.

Prior to the measurements all dispersed samples (both Cu and Cu_xZn_{1-x}) were held at –1 V vs. HgO/Hg in 0.1 M KOH solution for 1000 *sec* to reduce the surface oxides. After this, the samples were washed with ~ 250 mL of Milli-Q water and transferred into another three-electrode cell for voltammetric measurements.

Underpotential deposition of Pb on Cu was performed from a solution containing 10 mM $Pb(ClO_4)_2$, 100 mM $NaClO_4$, 1 mM KCl, pH 3. For dispersed Cu samples, the solution was stirred at 100 rpm during the measurements to ensure higher diffusion rates, which are significant for materials with large RSA, as was shown in our recent study [46]. For smooth deposits, the scan rate was 10 mV s^{-1}. For dispersed materials a lower scan rate of 0.5 mV s^{-1} was employed to ensure complete coverage of the surface with Pb adatoms. The obtained charges were recalculated into RSA values using a specific charge of 310 μC cm^{-2}, which is the value for a close packed Pb monolayer [20,58].

All glassware and electrochemical cells were thoroughly cleaned with hot concentrated sulfuric acid (Component-reactive, >94 %) and subsequently rinsed at least ten times with MilliQ water to ensure the effective removal of impurities. All the electrochemical measurements were performed using Metrohm Autolab potentiostat (PGSTAT302N) equipped with a linear scan generator module.

3. Results and discussion

3.1. *Phase composition*

XRD patterns of the Cu-Zn samples are presented in Fig. 1 (the information on the crystal structure of Cu and $Cu_{(Cl)}$ foams is provided in recent study [46]). A notable peak shift towards lower 2θ values on the patterns of two Cu-Zn samples is apparent, namely $Cu_{70}Zn_{30}$ foam and $Cu_{67}Zn_{33}$ foil. This peak shift is reflecting unit cell parameter increase with Zn content [59]. Peak positions for other four specimens are relatively close, which is in line with the similarity of their composition. During full-profile analysis it was found, that the best fitting is obtained when metallic foams are treated as two-phase mixtures of two solid solutions with f.c.c. structure (Cu structure type) because of the inability of standard peak shape functions to account for observed peak shape. For $Cu_{70}Zn_{30}$ foam unit cell parameters of these phases are $a = 3.666(1)$ Å and $a = 3.644(4)$ Å (weight fractions are 67 ± 6 wt% and 33 ± 7 wt%, respectively). For $Cu_{90}Zn_{10}$ foam unit cell parameters of these phases are $a = 3.634(1)$ Å and $a = 3.621(1)$ Å (74 ± 9 wt% and 26 ± 8 wt%, respectively). However, the unit cell parameters of the phases within each sample are close to each one, so the difference in chemical composition is minute. Significant peak broadening suggests a small size of the coherently scattering domains in both foams and coatings. The $Cu_{90}Zn_{10}$ smooth deposit represents a single-phase product ($a = 3.635$ (1) Å). The calculated lattice parameters of the $Cu_{90}Zn_{10}$ foam and $Cu_{90}Zn_{10}$ deposit are well consistent. The α-brass foils, which serve as the reference samples, exhibit larger lattice parameters ($Cu_{67}Zn_{33}$ foil: $a = 3.6984(2)$ Å; $Cu_{90}Zn_{10}$ foil: $a = 3.6402(1)$ Å) than their corresponding dispersed samples. This phenomenon can be explained by the presence of residual stresses resulting from the rolling process. These stresses cause changes in the lattice parameter relative to its equilibrium value [60].

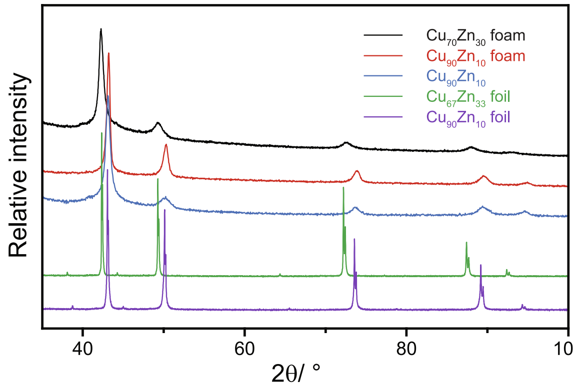

Fig. 1. XRD patterns of the samples under study. From top to bottom: $Cu_{70}Zn_{30}$ foam (black), $Cu_{90}Zn_{10}$ foam (red), $Cu_{90}Zn_{10}$ deposit (blue), $Cu_{67}Zn_{33}$ foil (green), $Cu_{90}Zn_{10}$ foil (violet). Low-intensity peaks on $Cu_{67}Zn_{33}$ foil and $Cu_{90}Zn_{10}$ foil are from residual CuK_β radiation. (For interpretation of the references to colour in this figure legend, the reader is referred to the web version of this article.)

3.2. *Surface morphology*

The SEM images of the deposited samples are presented in Fig. 2. The $Cu_{90}Zn_{10}$ sample obtained from pyrophosphate deposition solution is a smooth, non-porous coating composed of densely fused particles with submicron dimensions. The morphological features observable at low magnifications (left side panels of Fig. 2) are attributed to the topography of the copper foil used as the substrate. The metallic foams are significantly different morphologically. Firstly, the diameter of the macropores is notably larger in the case of $Cu_{70}Zn_{30}$, where the pores exceed 50 μm, whereas for the $Cu_{90}Zn_{10}$ foam, they do not exceed 20 μm. Secondly, the structure of the particles also differs markedly. The $Cu_{90}Zn_{10}$ foam consists of globular agglomerates with grain sizes of approximately 1 μm. In contrast, the particles in the $Cu_{70}Zn_{30}$ foam exhibit a pronounced dendritic structure, with the diameter of the dendrite branches not exceeding 200 nm.

3.3. *Voltammetric behavior*

The first issue to address is the stability of Cu-Zn materials in the electrolytes commonly used for cyclic voltammetry measurements aimed at determining the RSA. While Zn-rich brasses undergo a complex sequence of dezincification events at potentials significantly lower than those required for the oxidation of pure copper [61–63], α-brass begins to actively dissolve at potentials very close to those of pure copper oxidation [64]. It was shown that significant surface depletion of Zn during cycling is unlikely: spectro-electrochemical data indicate partial loss of Zn through dissolution as zincate ions, yet the surface composition of the brass is largely restored during the reverse cyclic voltammetry scan as the surface-oxidized species are reduced [65,66]. Consequently, cyclic voltammetry can typically be performed on both Cu and Cu-Zn samples within the same potential ranges.

Fig. 3 illustrates the anodic stability of pure copper (Cu and $Cu_{(Cl)}$ foams) and α-brass ($Cu_{70}Zn_{30}$ foam) samples in various electrolyte

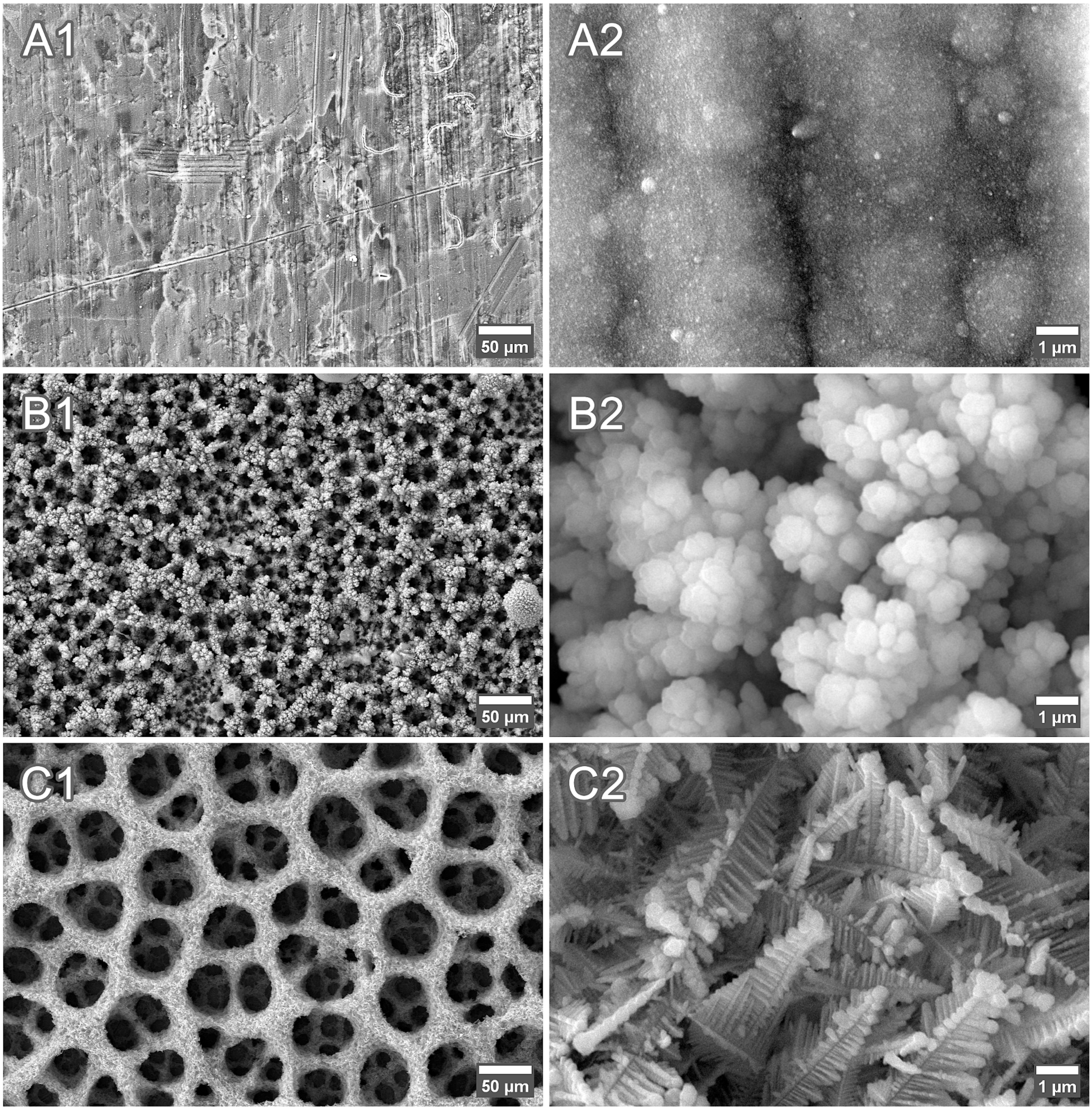

Fig. 2. SEM images of the samples under study. A1, A2 – $Cu_{90}Zn_{10}$ coating, B1, B2 – $Cu_{90}Zn_{10}$ foam, C1, *C*2 – $Cu_{70}Zn_{30}$ foam.

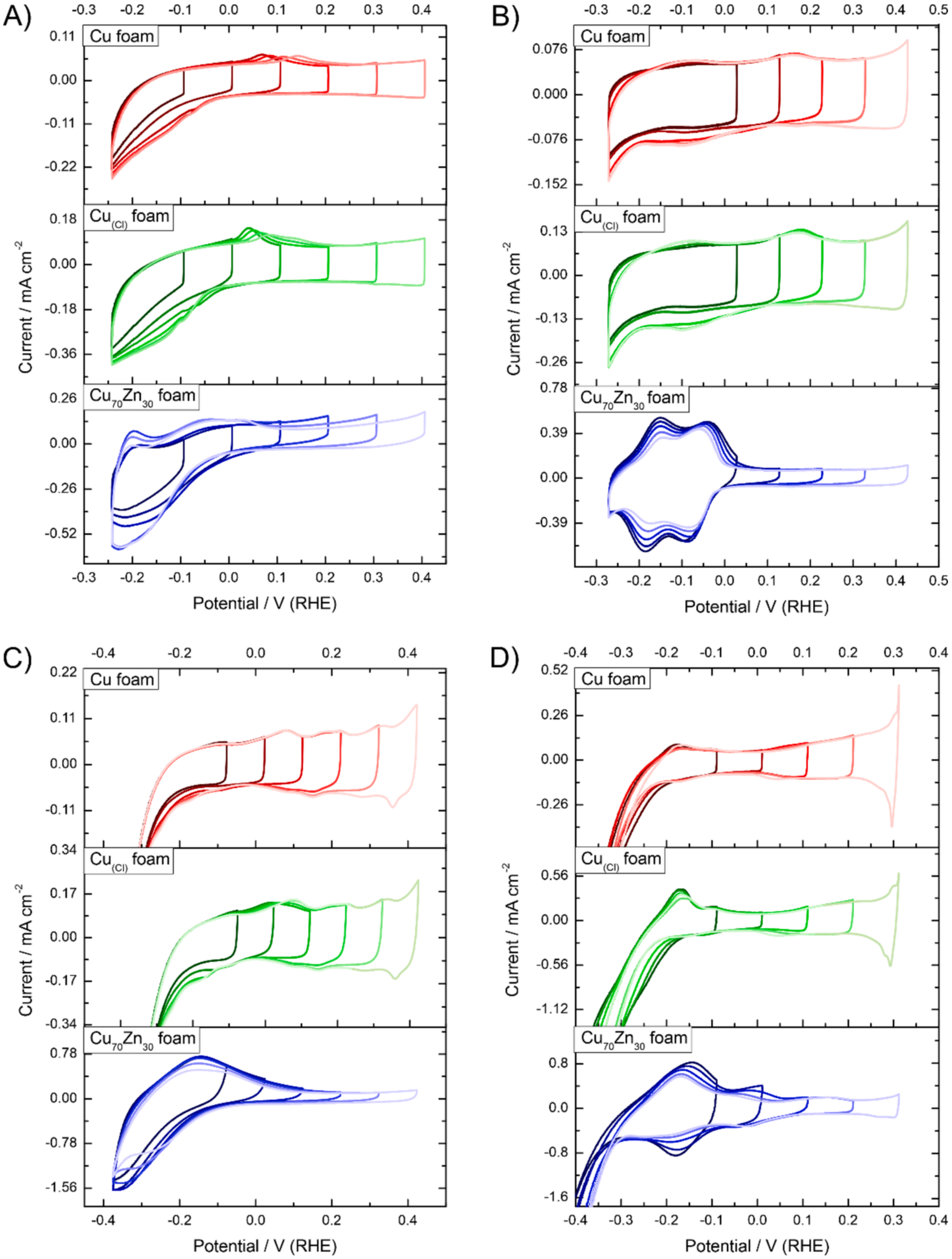

Fig. 3. CVs of Cu, $Cu_{(Cl)}$ and $Cu_{90}Zn_{30}$ foams in 0.5 M Na_2SO_4 (A), 0.5 M $KHCO_3$ (B), 0.1 M PBS (C) and 0.1 M KOH (D) solutions. Scan rate is 10 mV s^{-1}.

solutions: 0.5 M Na_2SO_4 (pH 5.9), 0.5 M $KHCO_3$ (pH 8.8), 0.1 M KOH (pH 13.0), and 0.1 M PBS (pH 7.4). High-surface area materials were chosen for these measurements to enhance the resolution of the characteristic voltammetric signatures. In all tested solutions, pure copper electrodes exhibit complex voltammetric behavior, characterized by the typical signatures associated with anion adsorption [14,16,17]. The copper foams display broad peaks within the potential range of −0.2 to + 0.2 V vs RHE, with the least stability observed in the 0.5 M Na_2SO_4 solution (Fig. 3A). This instability is likely due to local pH fluctuations in an unbuffered environment. Similarly, the voltammetric responses of $Cu_{70}Zn_{30}$ foam are also unstable in Na_2SO_4. Reduced stability of $Cu_{70}Zn_{30}$ foam is further observed in KOH solution (Fig. 3D), attributed to the dissolution of Zn as zincate ions under alkaline conditions [65].

In the bicarbonate solution, dispersed Cu samples reveal a pair of peaks at −0.1 V and a distinct anodic peak at 0.15 V (Fig. 3B), resembling the reported behavior of Cu(111) in $KHCO_3$ solutions [67]. In the same potential range of −0.1 to 0 V (RHE), the CVs of $Cu_{70}Zn_{30}$ foam exhibit two symmetric peaks followed by a significant reduction in current, suggesting passivation of the brass surface due to carbonate species adsorption. A somewhat analogous scenario is observed in PBS, where copper foams display multiple overlapping redox features related to phosphate species adsorption [68] (Fig. 3C). In contrast, for $Cu_{70}Zn_{30}$, the charge under the peaks appears to be greater, and the peaks shift to more negative potentials (−0.4 to −0.1 V vs RHE). This suggests that phosphate adsorption initiates at more negative potentials on the brass surface, leading to passivation, while the CVs at more positive potentials becomes relatively featureless. The adsorption of hydroxide species in alkaline solutions shows similar characteristics for both Cu and $Cu_{70}Zn_{30}$ samples, with OH_{ad} adsorption/desorption peaks located at −0.15 V for both pure metal and alloy (Fig. 3D).

The data presented in Fig. 3 indicate that the anodic stability limits for Cu and $Cu_{70}Zn_{30}$ foams are comparable, falling within the range of approximately 0.3 to 0.4 V vs RHE, depending on the electrolyte used. In $KHCO_3$, PBS, and KOH solutions, the onset of brass oxidation is observed to shift to more positive potentials, likely due to passivation effects induced by adsorption. The effect of phosphate as corrosion inhibitor for copper and brass materials is well-documented [69–71], and presumably similar effects are observed in carbonate and alkaline solutions.

Another significant finding is that the introduction of Zn into the copper structure effectively suppresses hydrogen evolution, in agreement with the trends in kinetic data reported for acidic environment [72]. This is evident as the hydrogen evolution currents begin to dominate the electrochemical response at more negative potentials, as illustrated in Fig. 3C and 3D.

Samples with relatively smooth surfaces, such as rolled metal foils, exhibit similar trends. However, due to their smaller RSA, the contribution of background currents becomes more pronounced, necessitating higher scan rates to obtain symmetric responses. This is illustrated in Fig. 4, which presents a series of CVs for commercial copper (Fig. 4A) and brass $Cu_{67}Zn_{33}$ (Fig. 4B) foils in four electrolyte solutions. Two potential intervals were examined: a broad range that includes the onset of hydrogen evolution and Cu_2O formation (indicated by green lines in Fig. 4), and a narrower, arbitrarily defined interval of 200 mV, where no distinct peaks related to the adsorption or desorption of electrolyte species are observed. The relatively featureless nature of these short-range intervals could be mistakenly interpreted as double-layer regions, where the phenomena are limited to double-layer charging. In Fig. 4, the short-range CVs are scaled by a factor indicated in the plots to align the current values between the short- and long-range CVs. This factor reflects the variation of the capacitance with the potential due to anion adsorption, which depends on both the potential and the electrolyte. For the copper foil, the difference in capacitance values between the short and long potential ranges varies significantly – from a factor of 2 in PBS to 20 in Na_2SO_4. For the α-brass $Cu_{67}Zn_{33}$, this factor is minimal in PBS (6) but reaches 15 and 17 in KOH and $KHCO_3$, respectively.

Alternative, electrochemical impedance spectroscopy (EIS) measurements could be used to quantify capacitance values for the samples in our study. However, for porous electrodes complex equivalent circuit modeling should be performed in order to extract physically meaningful estimates from the experimental data, while fitting to simple circuits with constant phase elements may result in unrealistic values of roughness factors [73,74]. For foils, the measured capacitance values by CV and EIS are sufficiently close (e.g. Cu foil: 46 $\mu F\ cm^{-2}$ (CV) vs. 44 $\mu F\ cm^{-2}$ (EIS), $Cu_{67}Zn_{33}$: 12 $\mu F\ cm^{-2}$ (CV) vs 7 $\mu F\ cm^{-2}$ (EIS), $Cu_{90}Zn_{10}$: 20 $\mu F\ cm^{-2}$ (CV) vs. 14 $\mu F\ cm^{-2}$ (EIS) in 0.1 M PBS solution), which corroborates the reliability of the performed estimates. The corresponding impedance spectra and the fits to the equivalent circuit are shown in Fig. S3, Table S2.

For all the explored samples, capacitance values across different potential ranges exhibit notable differences. Table 1 summarizes the capacitance values estimated from the CVs of various metal foils, including Cu, $Cu_{90}Zn_{10}$, and $Cu_{67}Zn_{33}$, as well as two types of dispersed copper samples: Cu and $Cu_{(Cl)}$ foams. The RSA of the copper foil was determined using lead UPD measurements, as detailed previously [46] (see Fig. 5, A-C). The roughness factors calculated were 1.3 for the Cu foil, 133 for the Cu foam, and 204 for the $Cu_{(Cl)}$ foam (Table 2). These roughness factors were applied to convert the estimated capacitance values into specific capacitance per unit of RSA. Due to the lack of

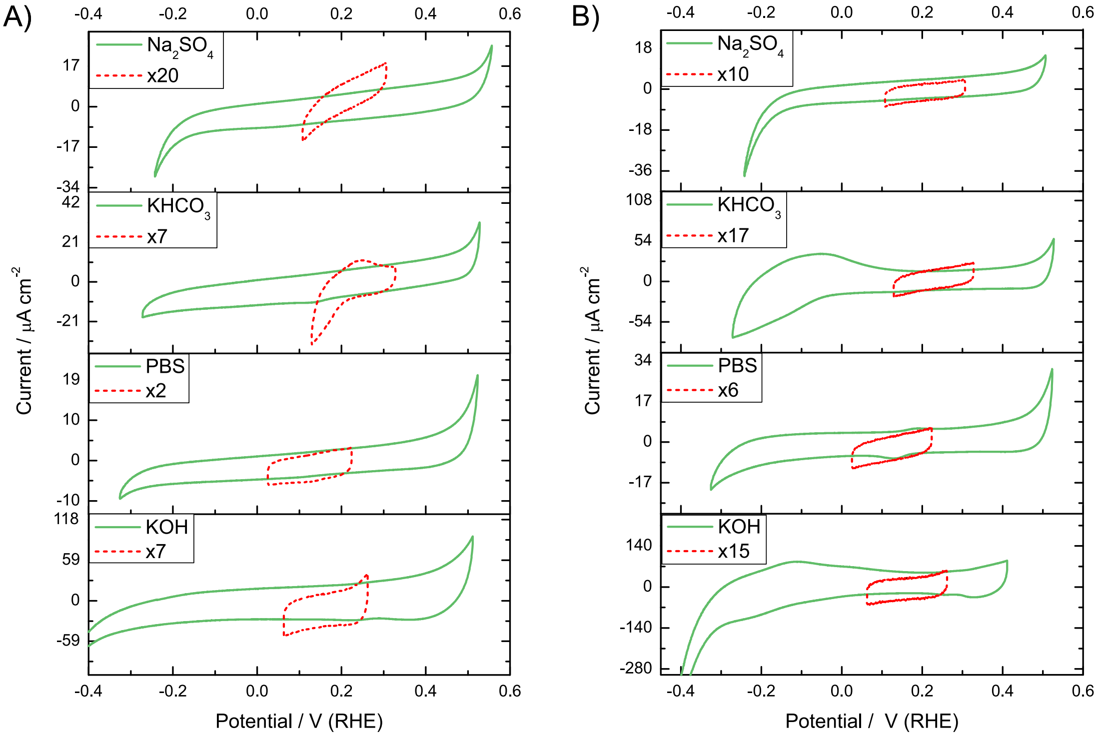

Fig. 4. CVs of Cu (A) and $Cu_{67}Zn_{33}$ (B) foils in 0.5 M Na_2SO_4, 0.5 M $KHCO_3$, 0.1 M PBS and 0.1 M KOH solutions in the wide and short potential ranges. The data for the short potential ranges is scaled by the factor, indicated in the plots. Scan rate is 50 mV s^{-1}.

Table 1
Capacitance values for Cu foil, Cu foam, $Cu_{(Cl)}$ foam, $Cu_{67}Zn_{33}$ and $Cu_{90}Zn_{10}$ foils in 0.5 M Na_2SO_4, 0.5 M $KHCO_3$, 0.1 M PBS and 0.1 M KOH solutions. For foams capacitances were calculated from CVs recorded at 10 mV s^{-1}, for Cu foil – at 50 mV s^{-1}, for Cu-Zn foils – at 100 mV s^{-1}.

Solution	Capacitance, μF cm^{-2}					Potential range, V
	Cu foil	Cu foam	$Cu_{(Cl)}$ foam	$Cu_{67}Zn_{33}$ foil	$Cu_{90}Zn_{10}$ foil	
Na_2SO_4	11	40	53	13	11	0.107 to 0.307
$KHCO_3$	22	44	70	14	15	0.128 to 0.328
PBS	46 (44)*	50	53	12 (7)	20 (14)	−0.075 to 0.125
KOH	52	91	96	32	29	0.062 to 0.262

*The numbers in parentheses refer to the capacitance values derived from EIS measurements (Fig. S3).

suitable electrochemical methods to determine roughness factors for the brass foils ($Cu_{90}Zn_{10}$ and $Cu_{67}Zn_{33}$), we assumed their roughness factor to be equivalent to that of the Cu foil, which is 1.3, given the similar production technique used for rolled foils.

The potential ranges presented in Table 1 were selected as 200 mV-wide intervals, corresponding to the minimal capacitance values observed in the CVs of copper and α-brass materials shown in Fig. 3. Several trends can be discerned from the data in Table 1. Firstly, there is a notable difference in capacitance values between smooth and dispersed materials. For example, in Na_2SO_4, $KHCO_3$, and KOH solutions, the specific capacitance of $Cu_{(Cl)}$ foam is significantly higher than that of Cu foil – by a factor of five in unbuffered Na_2SO_4, three times in $KHCO_3$, and 1.9 times in KOH. The smallest difference is observed in PBS, where the ratio is 1.15 (with specific capacitance values of 46, 50, and 53 μF cm^{-2} for Cu foil, Cu foam, and $Cu_{(Cl)}$ foam, respectively).

Similarly, in Na_2SO_4 and $KHCO_3$ solutions, there are differences in specific capacitance values between the more dispersed $Cu_{(Cl)}$ foam and the less dispersed Cu foam, although these differences are less pronounced (ranging from 1.4 to 1.7 times), with minimal variation noted in PBS. These observed differences can be attributed to the high sensitivity of adsorption energetics for OH*, HCO_3*, and HSO_4* species to the crystallographic orientation of the copper surfaces. Furthermore, the impact of impurities on anion adsorption may be more significant for smooth samples with lower RSA [75], potentially leading to reproducibility issues when weakly adsorbing species influence the measured capacitance values. Lastly, the rate of adsorption plays a crucial role. Higher scan rates are necessary for foils to achieve a high signal-to-background ratio, and slower adsorption kinetics may contribute to discrepancies in capacitance values between smooth and dispersed samples.

Another key observation is that the specific capacitance values for $Cu_{67}Zn_{33}$ and $Cu_{90}Zn_{10}$ foils differ significantly from those of pure copper, with the exception of the Na_2SO_4 electrolyte. However, Na_2SO_4 was identified as the least suitable electrolyte based on the comparative responses of smooth and dispersed samples, as the capacitance values for copper foil and foams were found to differ by 4–5 times in this medium (Table 1). In PBS, where measurements are least affected by variations in surface roughness, the capacitance values are 12 μF cm^{-2} for $Cu_{67}Zn_{33}$ and 20 μF cm^{-2} for $Cu_{90}Zn_{10}$ foils, while the specific capacitance for pure copper is 46 μF cm^{-2}. This analysis clearly indicates that using pure copper as a reference can lead to substantial errors – up to fourfold – in estimating the RSA of α-brass materials. Furthermore, there is no linear relationship (as shown in Fig. 6) between capacitance and copper content in the samples, except for the similarity observed in Na_2SO_4. The reduced capacitance observed in carbonate, phosphate, and hydroxide

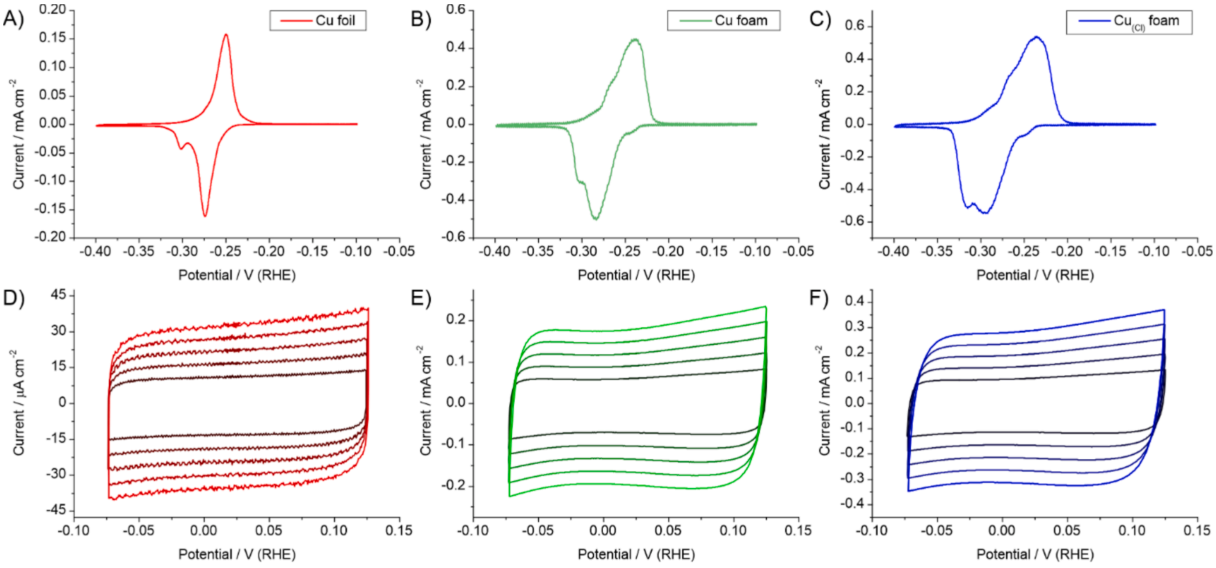

Fig. 5. Pb UPD CVs of Cu foil (A, scan rate is 10 mV s^{-1}), Cu foam (B, scan rate is 0.5 mV s^{-1}) and $Cu_{(Cl)}$ foam (C, scan rate is 0.5 mV s^{-1}) samples. CVs of Cu foil (D), Cu foam (E) and $Cu_{(Cl)}$ foam (F) in 0.1 M PBS solution (scan rates are 10, 15, 20, 25 and 30 mV s^{-1}).

Table 2
Roughness factors and BET surface areas for Cu and Cu-Zn samples under study.

Sample	Cu foil	Cu foam	$Cu_{(Cl)}$ foam	$Cu_{67}Zn_{33}$ foils	$Cu_{90}Zn_{10}$ foil	$Cu_{90}Zn_{10}$ deposit	$Cu_{90}Zn_{10}$ foam	$Cu_{70}Zn_{30}$ foam
Roughness factor from CV	1.3	133	204	1.3*	1.3*	6	117	167
BET surface area, m^2 g^{-1}	–	2.6 ± 0.4	–	–	–	–	–	13.7 ± 0.5
Surface area from CV	–	2.5	–	–	–	–	–	14.0

*Assumed.

solutions can be attributed to the passivation of the brass surface by poorly soluble zinc-based species. The observed nonlinear relationship between capacitance and zinc content in α-brass materials highlights how the degree of surface passivation by electrolyte anions is influenced by the concentration of zinc at the surface. Consequently, straightforward recalculations based on the specific capacitance of pure copper can introduce significant inaccuracies in the estimated surface area.

The results presented in Table 1 indicate that the 0.1 M PBS solution is the optimal choice for our study. The capacitance values for Cu foams and foils with varying roughness are remarkably similar, with differences not exceeding 12 %. In contrast, other electrolytes exhibit significantly larger variations in capacitance. To further validate these findings, we compared the RSA values derived from capacitive charges in the 0.1 M PBS solution with those obtained from lead UPD measurements. The charges were calculated by integrating and averaging the cathodic and anodic scans of the CVs in a short potential range (Fig. 5). As the charges show small but noticeable dependence on the scan rate (Fig. S4), the lowest scan rates were used to estimate the RSA.

The ratios of UPD charges to the capacitive charges for Cu foil, Cu foam, and $Cu_{(Cl)}$ foam in the 0.1 M PBS solution were closely aligned, with discrepancies remaining under 12 % (Table S3). This consistency supports the conclusion that capacitance values in PBS, at least under the specified experimental conditions, provide reliable estimates of RSA for copper electrodes.

Additionally, we determined the BET SSA for the Cu foam sample. Approximately 100 samples were electrodeposited under identical conditions, yielding around 100 mg of unsupported foam. Using the BET method, we calculated an SSA of 2.6 ± 0.4 $m^2\ g^{-1}$ (standard deviation). Fig. S2 shows the examples of respective isotherms. This value is consistent within the uncertainty range with the SSA of 2.5 $m^2\ g^{-1}$, calculated based on the determined roughness factor (133).

3.4. *RSA for α-brass samples*

The specific capacitance values of brass materials are influenced by the Cu:Zn ratio, making it essential for reference samples used in capacitance measurements to have closely matching compositions. In our study, we utilized two smooth brass foils with compositions of $Cu_{67}Zn_{33}$ and $Cu_{90}Zn_{10}$ (roughness factor of 1.3) as reference samples to estimate the capacitance values for the dispersed electrodeposited brass materials: highly dispersed $Cu_{70}Zn_{30}$ and $Cu_{90}Zn_{10}$ foams, as well as a smooth $Cu_{90}Zn_{10}$ coating. CV measurements for all brass materials were conducted within the optimized potential range of 0.045 to 0.245 V to ensure high reproducibility. The corresponding CVs are presented in Fig. S5.

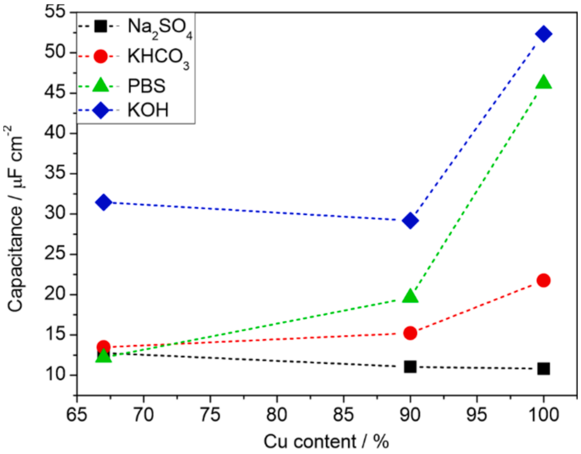

Fig. 6. Plot of specific capacitance values in 0.5 M Na_2SO_4 (black squares), 0.5 M $KHCO_3$ (red circles), 0.1 M PBS (green triangles) and 0.1 M KOH (blue rhombi) solutions vs. the Cu content. (For interpretation of the references to colour in this figure legend, the reader is referred to the web version of this article.)

To calculate the roughness factor for the $Cu_{70}Zn_{30}$ foam sample, we compared the charges from the CVs recorded in 0.1 M PBS for both the foam and the $Cu_{67}Zn_{33}$ foil samples. Additionally, we employed the BET method as an independent validation technique. The BET results yielded a specific surface area of 13.7 ± 0.5 $m^2\ g^{-1}$, which closely aligns with the RSA measurements that indicated a roughness factor of 167, corresponding to a SSA of 14.0 $m^2\ g^{-1}$ (Table 2). The near equivalence of these values suggests that the measurements are consistent within the experimental error.

Identical measurement procedures were applied to the $Cu_{90}Zn_{10}$ foam and $Cu_{90}Zn_{10}$ sample, using the $Cu_{90}Zn_{10}$ foil as a reference. The resulting roughness factors were 117 for the $Cu_{90}Zn_{10}$ foam, and 6 for the $Cu_{90}Zn_{10}$ deposit. These results confirm that our proposed methodology effectively provides reliable determinations of surface roughness for α-brass samples. While the BET method can be used to estimate the SSA for dispersed materials, the electrochemical method remains the preferred option for smooth deposits and other materials with low surface area.

4. Conclusions

Our investigation revealed that the capacitance values of Cu-Zn samples in aqueous solutions exhibit a significant non-linear dependence on α-brass composition, markedly differing from those of pure copper. To accurately estimate the RSA of brass samples, it is essential to carefully select both the electrolyte and the potential range for cyclic voltammetry measurements, as well as to utilize reference samples with similar (preferably identical) chemical compositions and known roughness.

By employing our developed procedure for estimating RSA, we successfully determined the roughness factors for brass samples electrodeposited onto copper substrates. The results highlight the potential uncertainties that can arise when using inappropriate reference samples for various brass compositions. For instance, utilizing the capacitance of pure copper to estimate the RSA of $Cu_{70}Zn_{30}$ foam yields a roughness factor that is nearly half (89 vs. 167) of that obtained with an appropriate reference sample under optimized conditions in PBS, which serves as a suitable electrolyte for these measurements.

Furthermore, the charge values are highly sensitive to the chosen potential range for cyclic voltammetry measurements. For example, the capacitance value for $Cu_{70}Zn_{30}$ foam in a $KHCO_3$ solution is 4.5 times greater in the potential range of −0.2 to 0.0 V (RHE) compared to the range of 0.1 to 0.3 V (RHE). Coupled with the risk of employing unsuitable reference samples, our findings indicate that errors in RSA estimation can approach an order of magnitude, which is unacceptable when comparing the electrocatalytic activity of different materials. This study underscores the critical need for employing appropriate surface area quantification techniques to mitigate uncertainties when reporting the activities of alloy-based materials in various electrochemical applications.

CRediT authorship contribution statement

Oleg I. Zaytsev: Writing – review & editing, Writing – original draft, Investigation, Formal analysis. **Margarita A. Belokozenko:** Investigation, Formal analysis. **Grigorii P. Lakienko:** Investigation, Formal analysis, Data curation. **Eduard E. Levin:** Writing – review & editing, Writing – original draft, Methodology, Investigation, Formal analysis. **Victoria A. Nikitina:** Writing – review & editing, Writing – original draft, Methodology, Conceptualization. **Sergey Y. Istomin:** Writing – review & editing, Supervision, Project administration, Funding acquisition.

Declaration of competing interest

The authors declare that they have no known competing financial interests or personal relationships that could have appeared to influence the work reported in this paper.

Acknowledgements

This study was supported by Russian Science Foundation (grant #22-13-00096, https://rscf.ru/project/22-13-00096/). The authors acknowledge partial support from M. V. Lomonosov Moscow State University Program of Development and from the Center for Energy Science and Technology, Skolkovo Institute of Science and Technology.

Appendix A. Supplementary data

Supplementary data to this article can be found online at https://doi.org/10.1016/j.jelechem.2024.118795.

References

[1] M. Du, X. Li, H. Pang, Q. Xu, Alloy electrocatalysts, Energy Chem 5 (2023) 100083, https://doi.org/10.1016/j.enchem.2022.100083.

[2] A. Raveendran, M. Chandran, R. Dhanusuraman, A comprehensive review on the electrochemical parameters and recent material development of electrochemical water splitting electrocatalysts, RSC Adv. 13 (2023) 3843–3876, https://doi.org/10.1039/d2ra07642j.

[3] G. Gao, G. Zhu, X. Chen, Z. Sun, A. Cabot, Optimizing Pt-Based Alloy Electrocatalysts for Improved Hydrogen Evolution Performance in Alkaline Electrolytes: A Comprehensive Review, ACS Nano 17 (2023) 20804–20824, https://doi.org/10.1021/acsnano.3c05810.

[4] M.A. Qadeer, X. Zhang, M.A. Farid, M. Tanveer, Y. Yan, S. Du, Z.-F. Huang, M. Tahir, J.-J. Zou, A review on fundamentals for designing hydrogen evolution electrocatalyst, J. Power Sources 613 (2024) 234856, https://doi.org/10.1016/j.jpowsour.2024.234856.

[5] Q. Wang, J. Xie, Y. Qin, Y. Kong, S. Zhou, Q. Li, Q. Sun, B. Chen, P. Xie, Z. Wei, S. Zhao, Recent Progress in High-Entropy Alloy Electrocatalysts for Hydrogen Evolution Reaction, Adv. Mater. Interfaces 11 (2024) 2301020, https://doi.org/10.1002/admi.202301020.

[6] X. Wang, Z. Li, Y. Qu, T. Yuan, W. Wang, Y. Wu, Y. Li, Review of Metal Catalysts for Oxygen Reduction Reaction: From Nanoscale Engineering to Atomic Design, Chem 5 (2019) 1486–1511, https://doi.org/10.1016/j.chempr.2019.03.002.

[7] C. Zhang, X. Shen, Y. Pan, Z. Peng, A review of Pt-based electrocatalysts for oxygen reduction reaction, Front. Energy 11 (2017) 268–285, https://doi.org/10.1007/s11708-017-0466-6.

[8] T. Wang, A. Chutia, D.J.L. Brett, P.R. Shearing, G. He, G. Chai, I.P. Parkin, Palladium alloys used as electrocatalysts for the oxygen reduction reaction, Energy Environ. Sci. 14 (2021) 2639–2669, https://doi.org/10.1039/d0ee03915b.

[9] J. He, N.J.J. Johnson, A. Huang, C.P. Berlinguette, Electrocatalytic Alloys for CO$_2$ Reduction, ChemSusChem 11 (2018) 48–57, https://doi.org/10.1002/cssc.201701825.

[10] L. Liu, H. Akhoundzadeh, M. Li, H. Huang, Alloy Catalysts for Electrocatalytic CO$_2$ Reduction, Small Methods 7 (2023) e2300482.

[11] W. Chen, Y. Wang, Y. Li, C. Li, Electrocatalytic CO$_2$ Reduction over Bimetallic Bi-Based Catalysts: A Review, CCS Chemistry 5 (2023) 544–567, https://doi.org/10.31635/ccschem.022.202202357.

[12] H. Yang, H. Chuai, Q. Meng, M. Wang, S. Zhang, X. Ma, Copper-based bimetallic electrocatalysts for CO$_2$ reduction: From mechanism understandings to product regulations, Mater. Rep.: Energy 3 (2023) 100174, https://doi.org/10.1016/j.matre.2022.100174.

[13] S. Trasatti, O.A. Petrii, Real surface area measurements in electrochemistry, J. Electroanal. Chem. 327 (1992) 353–376, https://doi.org/10.1016/0022-0728(92)80162-w.

[14] S. Härtinger, B. Pettinger, K. Doblhofer, Cathodic formation of a hydroxyde adsorbate on copper (111) electrodes in alkaline electrolyte, J. Electroanal. Chem. 397 (1995) 335–338, https://doi.org/10.1016/0022-0728(95)04297-5.

[15] V. Maurice, H.H. Strehblow, P. Marcus, In situ STM study of the initial stages of oxidation of Cu(111) in aqueous solution, Surf. Sci. 458 (2000) 185–194, https://doi.org/10.1016/s0039-6028(00)00442-8.

[16] H.Y.H. Chan, C.G. Takoudis, M.J. Weaver, Oxide Film Formation and Oxygen Adsorption on Copper in Aqueous Media As Probed by Surface-Enhanced Raman Spectroscopy, J. Phys. Chem. B 103 (1998) 357–365, https://doi.org/10.1021/jp983787c.

[17] J. Ambrose, R.G. Barradas, D.W. Shoesmith, Investigations of copper in aqueous alkaline solutions by cyclic voltammetry, J. Electroanal. Chem. 47 (1973) 47–64, https://doi.org/10.1016/s0022-0728(73)80344-4.

[18] G.M. Brisard, E. Zenati, H.A. Gasteiger, N. Markovic, P.N. Ross, Underpotential Deposition of Lead on Copper(111): A Study Using a Single-Crystal Rotating Ring Disk Electrode and ex Situ Low-Energy Electron Diffraction and Scanning tunneling Microscopy, Langmuir 11 (2002) 2221–2230, https://doi.org/10.1021/la00006a060.

[19] G.M. Brisard, E. Zenati, H.A. Gasteiger, N.M. Marković, P.N. Ross, Underpotential Deposition of Lead on Cu(100) in the Presence of Chloride: Ex-Situ Low-Energy Electron Diffraction, Auger Electron Spectroscopy, and Electrochemical Studies, Langmuir 13 (1997) 2390–2397, https://doi.org/10.1021/la960999x.

[20] H. Siegenthaler, K. Jüttner, Voltammetric investigation of lead adsorption on Cu (111) single crystal substrates, J. Electroanal. Chem. 163 (1984) 327–343, https://doi.org/10.1016/s0022-0728(84)80060-1.

[21] K.J. Rawlings, M.J. Gibson, P.J. Dobson, The epitaxial growth of lead and thallium on (111) silver and copper, J. Phys. D: Appl. Phys. 11 (1978) 2059–2070, https://doi.org/10.1088/0022-3727/11/14/015.

[22] S.A.S. Machado, L.A. Avaca, The hydrogen evolution reaction on nickel surfaces stabilized by H-absorption, Electrochim. Acta 39 (1994) 1385–1391, https://doi.org/10.1016/0013-4686(94)e0003-i.

[23] M. Grden, M. Alsabet, G. Jerkiewicz, Surface science and electrochemical analysis of nickel foams, ACS Appl. Mater. Interfaces 4 (2012) 3012–3021, https://doi.org/10.1021/am300380m.

[24] J. van Drunen, B. Kinkead, M.C. Wang, E. Sourty, B.D. Gates, G. Jerkiewicz, Comprehensive structural, surface-chemical and electrochemical characterization of nickel-based metallic foams, ACS Appl. Mater. Interfaces 5 (2013) 6712–6722, https://doi.org/10.1021/am401606n.

[25] D.S. Hall, C. Bock, B.R. MacDougall, An Oxalate Method for Measuring the Surface Area of Nickel Electrodes, J. Electrochem. Soc. 161 (2014) H787–H795, https://doi.org/10.1149/2.0711412jes.

[26] M. Wasberg, G. Horányi, The reversibility and overlapping of hydrogen and oxygen adsorption in the “double-layer” region of rhodized electrodes in H$_2$SO$_4$ solutions (the decomposition of water molecules on rhodium surfaces), J. Electroanal. Chem. 386 (1995) 213–219, https://doi.org/10.1016/0022-0728(94)03795-5.

[27] S. Hadzi-Jordanov, H. Angerstein-Kozlowska, M. Vuković, B.E. Conway, Reversibility and Growth Behavior of Surface Oxide Films at Ruthenium Electrodes, J. Electrochem. Soc. 125 (2019) 1471–1480, https://doi.org/10.1149/1.2131698.

[28] Y. Yoon, B. Yan, Y. Surendranath, Suppressing Ion Transfer Enables Versatile Measurements of Electrochemical Surface Area for Intrinsic Activity Comparisons, J. Am. Chem. Soc. 140 (2018) 2397–2400, https://doi.org/10.1021/jacs.7b10966.

[29] A. Czerwinski, J. Sobkowski, Electrosorption of CO and CO$_2$ on Pt-Rh Alloy Electrodes, Anal. Lett. 17 (2006) 2175–2181, https://doi.org/10.1080/00032718408065364.

[30] F. Kadirgan, B. Beden, J.M. Leger, C. Lamy, Synergistic effect in the electrocatalytic oxidation of methanol on platinum+palladium alloy electrodes, J. Electroanal. Chem. 125 (1981) 89–103, https://doi.org/10.1016/s0022-0728(81)80326-9.

[31] M. Łukaszewski, A. Czerwiński, Electrochemical preparation and characterization of thin deposits of Pd-noble metal alloys, Thin Solid Films 518 (2010) 3680–3689, https://doi.org/10.1016/j.tsf.2009.10.008.

[32] Y. Wang, T. Gong, M. Lee, A.S. Hall, Structural transformations of metal alloys under electrocatalytic conditions, Curr. Opin. Electrochem. 30 (2021) 100796, https://doi.org/10.1016/j.coelec.2021.100796.

[33] L. Cao, Z. Zhao, Z. Liu, W. Gao, S. Dai, J. Gha, W. Xue, H. Sun, X. Duan, X. Pan, T. Mueller, Y. Huang, Differential Surface Elemental Distribution Leads to Significantly Enhanced Stability of PtNi-Based ORR Catalysts, Matter 1 (2019) 1567–1580, https://doi.org/10.1016/j.matt.2019.07.015.

[34] H. Liao, A. Fisher, Z.J. Xu, Surface Segregation in Bimetallic Nanoparticles: A Critical Issue in Electrocatalyst Engineering, Small 11 (2015) 3221–3246, https://doi.org/10.1002/smll.201403380.

[35] I.M. Badawy, A.M. Ismail, G.E. Khedr, M.M. Taha, N.K. Allam, Selective electrochemical reduction of CO$_2$ on compositionally variant bimetallic Cu-Zn electrocatalysts derived from scrap brass alloys, Sci. Rep. 12 (2022) 13456, https://doi.org/10.1038/s41598-022-17317-6.

[36] M. Fan, M.J. Eslamibidgoli, X. Zhu, S. Garbarino, A.C. Tavares, M. Eikerling, D. Guay, Understanding the Improved Activity of Dendritic Sn$_1$Pb$_3$ Alloy for the CO$_2$ Electrochemical Reduction: A Computational-Experimental Investigation, ACS Catal. 10 (2020) 10726–10734, https://doi.org/10.1021/acscatal.0c01785.

[37] Y. Baek, H. Song, D. Hong, S. Wang, S. Lee, Y.-C. Joo, G.-D. Lee, J. Oh, Electrochemical carbon dioxide reduction on copper–zinc alloys: ethanol and ethylene selectivity analysis, J. Mater. Chem. A 10 (2022) 9393–9401, https://doi.org/10.1039/d1ta10345h.

[38] M. Guo, X. Li, Y. Huang, L. Li, J. Li, Y. Lu, Y. Xu, L. Zhang, CO$_2$-Induced Fibrous Zn Catalyst Promotes Electrochemical Reduction of CO$_2$ to CO, Catalysts 11 (2021) 477, https://doi.org/10.3390/catal11040477.

[39] A.H.M. da Silva, S.J. Raaijman, C.S. Santana, J.M. Assaf, J.F. Gomes, M.T.M. Koper, Electrocatalytic CO$_2$ reduction to C$_{2+}$ products on Cu and Cu$_x$Zn$_y$ electrodes: Effects of chemical composition and surface morphology, J. Electroanal. Chem. 880 (2021) 114750, https://doi.org/10.1016/j.jelechem.2020.114750.

[40] J. Zhang, C. Guo, S. Fang, X. Zhao, L. Li, H. Jiang, Z. Liu, Z. Fan, W. Xu, J. Xiao, M. Zhong, Accelerating electrochemical CO$_2$ reduction to multi-carbon products via asymmetric intermediate binding at confined nanointerfaces, Nat. Commun. 14 (2023) 1298, https://doi.org/10.1038/s41467-023-36926-x.

[41] S. Zhen, G. Zhang, D. Cheng, H. Gao, L. Li, X. Lin, Z. Ding, Z.J. Zhao, J. Gong, Nature of the Active Sites of Copper Zinc Catalysts for Carbon Dioxide Electroreduction, Angew. Chem. Int. Ed. Engl. 61 (2022) e202201913.

[42] L. Wan, X. Zhang, J. Cheng, R. Chen, L. Wu, J. Shi, J. Luo, Bimetallic Cu–Zn Catalysts for Electrochemical CO$_2$ Reduction: Phase-Separated versus Core-Shell Distribution, ACS Catal. 12 (2022) 2741–2748, https://doi.org/10.1021/acscatal.1c05272.

[43] H.S. Jeon, J. Timoshenko, F. Scholten, I. Sinev, A. Herzog, F.T. Haase, B. Roldan Cuenya, Operando Insight into the Correlation between the Structure and Composition of CuZn Nanoparticles and Their Selectivity for the Electrochemical CO_2 Reduction, J. Am. Chem. Soc. 141 (2019) 19879–19887, https://doi.org/10.1021/jacs.9b10709.

[44] D. Karapinar, C.E. Creissen, J.G. Rivera de la Cruz, M.W. Schreiber, M. Fontecave, Electrochemical CO_2 Reduction to Ethanol with Copper-Based Catalysts, ACS Energy Lett. 6 (2021) 694–706, https://doi.org/10.1021/acsenergylett.0c02610.

[45] S. Bae, S.Y. Hwang, G. Yun, Y. Gwon, S.Y. Kim, C.K. Rhee, Y. Sohn, Electrocatalytic CO2 Reduction for Dynamic C_1, C_2, and C_{3+} Chemistry over Electrodeposited Zn on Cu and CuZn Mesh Supports, Energy Fuels (2024), https://doi.org/10.1021/acs.energyfuels.4c02546.

[46] E.E. Levin, D.A. Morozov, V.V. Frolov, N.A. Arkharova, D.N. Khmelenin, E. V. Antipov, V.A. Nikitina, Roughness Factors of Electrodeposited Nanostructured Copper Foams, Nanomaterials 13 (2023) 3011, https://doi.org/10.3390/nano13233011.

[47] H.M. Otte, Lattice Parameter Determinations with an X-Ray Spectrogoniometer by the Debye-Scherrer Method and the Effect of Specimen Condition, J. Appl. Phys. 32 (1961) 1536–1546, https://doi.org/10.1063/1.1728392.

[48] S. Shimizu, Y. Murakami, S. Kachi, Lattice Softening and Martensitic Transformation in Cu–Ni–Zn β Phase Alloys, J. Phys. Soc. Jpn. 41 (1976) 79–84, https://doi.org/10.1143/jpsj.41.79.

[49] J.K. Brandon, R.Y. Brizard, P.C. Chieh, R.K. McMillan, W.B. Pearson, New refinements of the γ brass type structures Cu_5Zn_8, Cu_5Cd_8 and Fe_3Zn_{10}, Acta Crystallogr., Sect. B: Struct. Crystallogr. Cryst. Chem. 30 (1974) 1412–1417, https://doi.org/10.1107/s0567740874004997.

[50] H.M. Rietveld, A profile refinement method for nuclear and magnetic structures, J. Appl. Crystallogr. 2 (1969) 65–71, https://doi.org/10.1107/s0021889869006558.

[51] R.J. Hill, C.J. Howard, Quantitative phase analysis from neutron powder diffraction data using the Rietveld method, J. Appl. Crystallogr. 20 (1987) 467–474, https://doi.org/10.1107/s0021889887086199.

[52] L.A. Solovyov, Full-profile refinement by derivative difference minimization, J. Appl. Crystallogr. 37 (2004) 743–749, https://doi.org/10.1107/s0021889804015638.

[53] L.A. Solovyov, Full-profile refinement by derivative difference minimization, Erratum. *J. Appl. Crystallogr.* 38 (2005) 401, https://doi.org/10.1107/s0021889805004899.

[54] A. Le Bail, Whole powder pattern decomposition methods and applications: A retrospection, Powder Diffr. 20 (2012) 316–326, https://doi.org/10.1154/1.2135315.

[55] K.J.J. Mayrhofer, A.S. Crampton, G.K.H. Wiberg, M. Arenz, Analysis of the Impact of Individual Glass Constituents on Electrocatalysis on Pt Electrodes in Alkaline Solution, J. Electrochem. Soc. 155 (2008) P78, https://doi.org/10.1149/1.2904882.

[56] K.J.J. Mayrhofer, G.K.H. Wiberg, M. Arenz, Impact of Glass Corrosion on the Electrocatalysis on Pt Electrodes in Alkaline Electrolyte, J. Electrochem. Soc. 155 (2008) P1, https://doi.org/10.1149/1.2800752.

[57] A. Tiwari, T. Maagaard, I. Chorkendorff, S. Horch, Effect of Dissolved Glassware on the Structure-Sensitive Part of the Cu(111) Voltammogram in KOH, ACS Energy Lett. 4 (2019) 1645–1649, https://doi.org/10.1021/acsenergylett.9b01064.

[58] A. Bewick, J. Jovićević, B. Thomas, Phase formation in the underpotential deposition of metals, Faraday Symp. Chem. Soc. 12 (1977) 24–35, https://doi.org/10.1039/fs9771200024.

[59] W. Hume-Rothery, G.F. Lewin, P.W. Reynolds, The lattice spacings of certain primary solid solutions in silver and copper, Proc. R. Soc. London, Ser. A 157 (1936) 167–183, https://doi.org/10.1098/rspa.1936.0186.

[60] R. Delhez, T. de Keijser, E.J. Mittemeijer, J.I. Langford, Size and Strain Parameters from Peak Profiles: Sense and Nonsense, Aust. J. Phys. 41 (1988) 213, https://doi.org/10.1071/ph880213.

[61] H.W. Pickering, Formation of New Phases during Anodic Dissolution of Zn-Rich Cu-Zn Alloys, J. Electrochem. Soc. 117 (1970) 8, https://doi.org/10.1149/1.2407450.

[62] A.H. Taylor, The Corrosion Behavior of Cu and Naval Brass in 0.5M NaCl Solutions at Ambient Temperature, J. Electrochem. Soc. 118 (1971) 854, https://doi.org/10.1149/1.2408204.

[63] R.C. Newman, T. Shahrabi, K. Sieradzki, Direct electrochemical measurement of dezincification including the effect of alloyed arsenic, Corr. Sci. 28 (1988) 873–886, https://doi.org/10.1016/0010-938x(88)90036-4.

[64] J. Stevanović, L.J. Skibina, M. Stefanović, A. Despić, V.D. Jović, Phase-structure analysis of brass by anodic linear-sweep voltammetry, J. Appl. Electrochem. 22 (1992) 172–178, https://doi.org/10.1007/bf01023820.

[65] B.S. Kim, T. Piao, S.N. Hoier, S.M. Park, In situ spectro-electrochemical studies on the oxidation mechanism of brass, Corros. Sci. 37 (1995) 557–570, https://doi.org/10.1016/0010-938x(94)00147-x.

[66] F. Wiame, B. Salgin, J. Swiatowska-Mrowiecka, V. Maurice, P. Marcus, Brass Surface Nanochemistry: The Role of Alloying Cu with Zn, J Phys. Chem. C 112 (2008) 7540–7543, https://doi.org/10.1021/jp801739b.

[67] P.K.J. Schouten, E.P. Gallent, M.T.M. Koper, The electrochemical characterization of copper single-crystal electrodes in alkaline media, J. Electroanal. Chem. 699 (2013) 6–9, https://doi.org/10.1016/j.jelechem.2013.03.018.

[68] P. Sebastián-Pascual, M. Escudero-Escribano, Addressing the Interfacial Properties for CO Electroreduction on Cu with Cyclic Voltammetry, ACS Energy Lett. 5 (2019) 130–135, https://doi.org/10.1021/acsenergylett.9b02456.

[69] G. Kılınççeker, M. Erbil, The effect of phosphate ions on the electrochemical behaviour of brass in sulphate solutions, Mater. Chem. Phys. 119 (2010) 30–39, https://doi.org/10.1016/j.matchemphys.2009.07.040.

[70] L. Yohai, M. Vázquez, M.B. Valcarce, Brass corrosion in tap water distribution systems inhibited by phosphate ions, Corrosion Sci. 53 (2011) 1130–1136, https://doi.org/10.1016/j.corsci.2010.12.005.

[71] X.S. Du, Y.J. Su, J.X. Li, L.J. Qiao, W.Y. Chu, Inhibitive effects and mechanism of phosphates on the stress corrosion cracking of brass in ammonia solutions, Corrosion Sci. 60 (2012) 69–75, https://doi.org/10.1016/j.corsci.2012.04.011.

[72] S. Trasatti, Work function, electronegativity, and electrochemical behaviour of metals, J. Electroanal. Chem. 39 (1972) 163–184, https://doi.org/10.1016/s0022-0728(72)80485-6.

[73] E. Rouya, S. Cattarin, M.L. Reed, R.G. Kelly, G. Zangari, Electrochemical Characterization of the Surface Area of Nanoporous Gold Films, J. Electrochem. Soc. 159 (2012) K97–K102, https://doi.org/10.1149/2.097204jes.

[74] B. Serapinienė, L. Gudavičiūtė, S. Tutlienė, A. Grigucevičienė, A. Selskis, J. Juodkazytė, R. Ramanauskas, On the electrochemically active surface area determination of electrodeposited porous Cu 3D nanostructures, Coatings 13 (2023) 1335, https://doi.org/10.3390/coatings13081335.

[75] N. Fröhlich, J. Fernández-Vidal, F.V. Mascaró, A.J. Shih, M. Luo, M.T.M. Koper, Effect of trace impurities in perchloric acid on blank voltammetry of Pt(111), Electrochim. Acta 466 (2023) 143035, https://doi.org/10.1016/j.electacta.2023.143035.